

Scaling Crystal Structure Relaxation with a Universal Trustworthy Deep Generative Model

Ziduo Yang^{1,2†}, Yiming Zhao^{2†}, Xiaoqing Liu², Xiuying Zhang², Yifan Li², Qiujiu Lyu^{1,2}, Calvin Yu-Chian Chen^{1,3,4,5,6*} and Lei Shen^{2*}

¹Artificial Intelligence Medical Research Center, School of Intelligent Systems Engineering, Shenzhen Campus of Sun Yat-sen University, Shenzhen, 518107, China.

²Department of Mechanical Engineering, National University of Singapore, 9 Engineering Drive 1, 117575, Singapore.

³AI for Science (AI4S)-Preferred Program, Peking University Shenzhen Graduate School, Shenzhen, 518055, China.

⁴School of Electronic and Computer Engineering, Peking University Shenzhen Graduate School, Shenzhen, 518055, China.

⁵Department of Medical Research, China Medical University Hospital, Taichung, 40447, Taiwan.

⁶Department of Bioinformatics and Medical Engineering, Asia University, Taichung, 41354, Taiwan.

*Corresponding author(s). E-mail(s): cy@pku.edu.cn; shenlei@nus.edu.sg;

Contributing authors: yangzd@mail2.sysu.edu.cn; yiming.zhao@u.nus.edu; liuxiaoq1994@gmail.com; phyxyz@nus.edu.sg; e0576095@u.nus.edu; lvqj5@mail2.sysu.edu.cn;

†These authors contributed equally to this work.

Abstract

The evolution of AI and high-throughput technologies has boosted a rapid increase in the number of new materials, challenging our computational ability to comprehensively analyze their properties. Relaxed crystal structures often serve as the foundational basis for further property calculations. However, determining equilibrium structures traditionally involves computationally expensive iterative calculations. Here, we develop DeepRelax, an efficient deep generative model designed for rapid structural relaxation without any iterative process. DeepRelax learns the equilibrium structural distribution, enabling it to predict relaxed structures directly from their unrelaxed counterparts. The ability to perform structural relaxation in just a few hundred milliseconds per structure, combined with the scalability of parallel processing, makes DeepRelax particularly useful for large-scale virtual screening. To demonstrate the universality of DeepRelax, we benchmark it against three different databases of X-Mn-O oxides, Materials Project, and Computational 2D Materials Database with various types of materials. In these tests, DeepRelax exhibits both high accuracy and efficiency in structural relaxation, as further validated by DFT calculations. Finally, we integrate DeepRelax with an implementation of uncertainty quantification, enhancing its reliability and trustworthiness in material discovery. This work provides an efficient and trustworthy method to significantly accelerate large-scale computations, offering substantial advancements in the field of computational materials science.

Keywords: Materials Discovery, Structural Relaxation, Graph Neural Networks, Uncertainty Quantification

1 Introduction

The discovery of new materials has significantly accelerated in the past decade, owing in part to the expansion of crystal structure databases by high-throughput density functional theory (DFT) calculations[1–4] and advanced machine learning (ML) algorithms [5–8]. For example, very recently, around 2.2 million new crystal materials have been discovered by Google DeepMind using graph neural networks[9].

Structural relaxation, the first step and foundation for further computationally analyzing properties of any new materials, is typically achieved using iterative optimization, such as *ab initio* methods or ML algorithms as shown in Figure 1 (a). For example, each iteration in DFT calculations involves solving the Schrödinger equation to determine the electronic density distribution, from which the total energy of the system can be calculated. The forces on each atom, derived from differentiating this energy with respect to atomic

positions, guide atomic movements to lower the system’s energy, typically using optimization algorithms. Despite its effectiveness, the high computational demands and poor scalability of DFT limit its widespread application across high-dimensional chemical and structural spaces[10], such as the structural relaxation of the aforementioned 2.2 million new crystals or complex chemical reaction surfaces or doped semiconductor interfaces.

On the other hand, machine learning (ML) has emerged as a promising alternative for predicting relaxed structures[10–18]. As conventional iterative optimization, iterative ML approaches[10–14, 17, 18] utilize surrogate ML models to approximate energy and forces at each iteration, as shown in Figure 1 (a), thereby circumventing the need to solve the computationally intensive Schrödinger equation. These ML models can retain DFT-level accuracy by training on extensive databases containing detailed information on structural relaxations, including energy, forces, and stress.

However, there are two primary challenges in current *iterative* ML structural optimizers: training data limitations and non-scalability. Their training dataset must include full or partial intermediate steps of DFT relaxation. However, almost all publicized material databases, such as ICSD[19] and 2DMatPedia[4], do not provide such structural information, potentially limiting the application of iterative ML methods. The other challenge is that the large-scale parallel processing capability of iterative ML methods is limited due to their step-by-step nature. To address this, Yoon[16] and Kim[15] conceptually proposed *direct* ML approaches to predict the final relaxed structures directly from their unrelaxed versions. However, these approaches have only been validated on specific datasets or systems, and their universal applicability to diverse datasets or systems remains unproven.

In this work, we develop a scalable, universal, and trustworthy deep generative model for fast structural relaxation, DeepRelax, by learning from the structural relationships between unrelaxed and relaxed crystals. DeepRelax requires only the initial crystal structures to predict equilibrium structures in just a few hundred milliseconds on a single GPU. Furthermore, DeepRelax can efficiently handle multiple crystal structures in parallel by organizing them into mini-batches for simultaneous processing. This capability is especially advantageous in large-scale virtual screening, where rapid assessment of numerous unknown crystal configurations is essential. Most importantly, DeepRelax employs an uncertainty quantification method to assess the reliability of the predicted structure, enabling the identification and exclusion of predictions that are likely to be unreliable. We evaluate DeepRelax across three different datasets, including diverse 3D and 2D materials: the Materials Project (MP)[20], X-Mn-O oxides[15, 21], and the Computational 2D Materials Database (C2DB)[22–24]. DeepRelax not only demonstrates superior performance compared to other direct ML methods but also exhibits competitive accuracy to the leading iterative ML model, M3GNet[11], while being approximately 100 times faster in terms of speed. Moreover, we conduct DFT

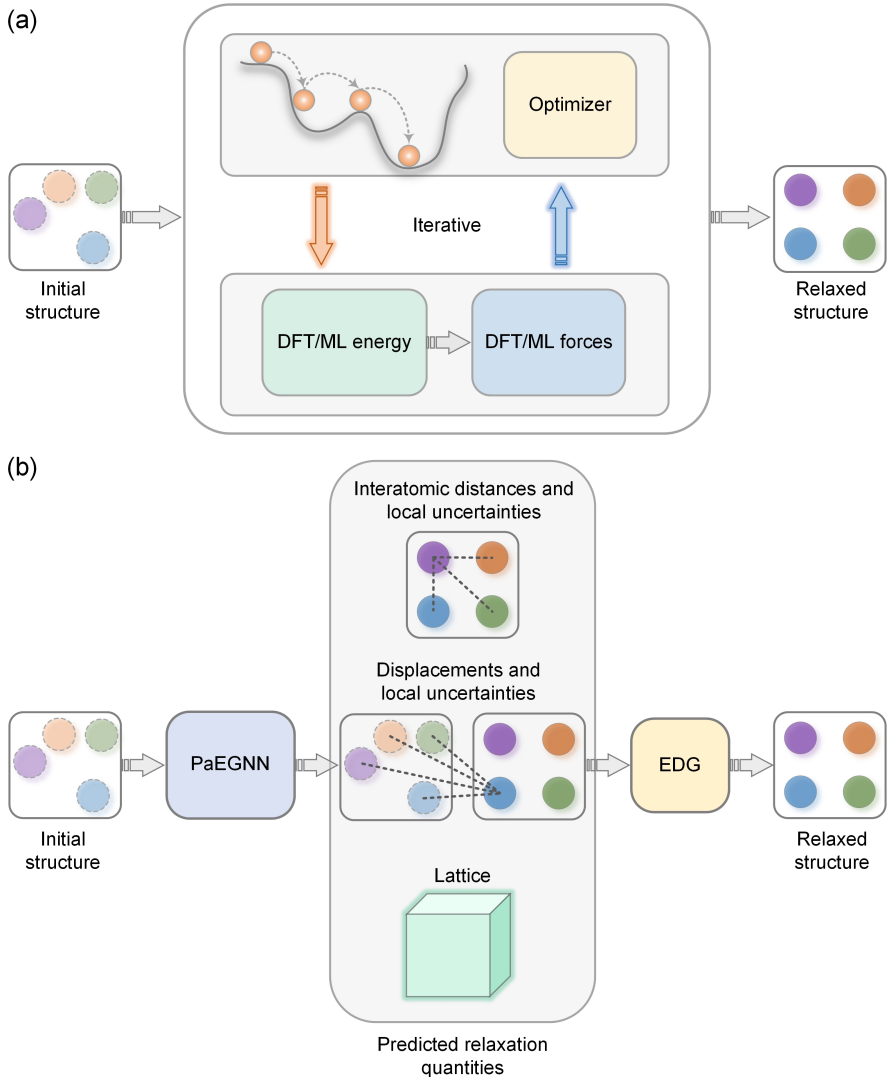
4 *DeepRelax*

Fig. 1 An overview of ML methods for crystal structure relaxation. Panel (a) depicts iterative ML methods that iteratively estimate energy and force to determine the equilibrium structure. Panel (b) illustrates our proposed DeepRelax method, which directly predicts the equilibrium structure without the iterative process.

calculations to assess the energy of DeepRelax’s predicted structures, confirming our model’s ability to identify energetically favorable configurations. Finally, we would like to highlight that the aim of using DeepRelax is not to replace DFT relaxation, but to make the predicted structures close to the final relaxed configuration. Thus, the DFT method can rapidly complete the relaxation with only a few steps, significantly speeding up the traditional *ab initio* relaxation process, especially for complex structures.

2 Results

2.1 DeepRelax architecture

DeepRelax emerges as a solution to the computational bottlenecks faced in DFT methods for crystal structure relaxation. The foundation of DeepRelax is a periodicity-aware equivariant GNN (PaEGNN). This network is designed for handling periodic boundary conditions (PBCs) explicitly and ensures equivariance to actively explore crystal symmetries, thereby offering a more enriched geometrical representation for crystal structures. Figure 1 (b) shows the workflow of DeepRelax, which takes a crystal structure as input and uses PaEGNN to predict the relaxation quantities. These quantities include interatomic distances in the relaxed structure and their associated local uncertainties (i.e., bond-level uncertainties), displacements between the initial and relaxed structures (also quantified with local uncertainties), and lattice parameters of the relaxed structure. By aggregating these local uncertainties, one can determine the global uncertainty of the predicted structure. The inclusion of uncertainties in these predictions offers insights into the confidence and reliability of the model’s outputs. Finally, DeepRelax employs a numerical Euclidean distance geometry (EDG) solver to determine the relaxed structure that satisfies the relaxation quantities. For more details, please refer to **Section 4**.

2.2 Benchmark on X-Mn-O dataset

For our initial benchmarking, we utilize the X-Mn-O dataset, a hypothetical elemental substitution database previously employed for photoanode application studies[21, 25]. This dataset derives from the MP database, featuring prototype ternary structures that undergo elemental substitution with X elements (Mg, Ca, Ba, and Sr). It consists of 28,579 data pairs, with each comprising an unrelaxed structure and its corresponding relaxed state. The dataset is divided into training ($N = 22,863$), validation ($N = 2,857$), and test ($N = 2,859$) sets, adhering to an 8:1:1 ratio. As illustrated in **Supplementary Materials (SM)**, Figure S1, there are significant structural differences between the unrelaxed and relaxed structures within this dataset.

We conduct a comparative analysis of DeepRelax against the state-of-the-art (SOTA) benchmark model, Cryslator[15]. Additionally, we incorporate two types of equivariant graph neural networks—PAINN[26] and EGNN[27]—into our analysis (see **Subsection 4.8** for the details). The choice of equivariant models is informed by recent reports highlighting their accuracy in direct coordinate prediction for structural analysis[27–29]. To ensure a fair comparison, we use the same training, validation, and testing sets across all models. As a baseline measure, we introduce a Dummy model, which simply returns the input initial structure as its output. This serves as a control reference in our evaluation process.

To evaluate model performance, we use the MAE of Cartesian coordinates, bond lengths, lattice parameters, and cell volume to measure the consistency

between predicted and ground-truth relaxed structures. Additionally, we calculate the match rate—a measure of how closely predicted relaxed structures align with their ground truth counterparts within a defined tolerance, as determined by Pymatgen[1]. Detailed descriptions of these metrics are provided in **Subsection 4.10**.

Table 1 presents the comparative results, showing that DeepRelax greatly outperforms other baselines. Notably, DeepRelax shows a remarkable improvement in prediction accuracy over the Dummy model, with enhancements of 63.06%, 68.30%, 71.49%, 89.63%, and 30.71% across coordinates, bond lengths, lattice, cell volumes, and match rate, respectively. Moreover, DeepRelax surpasses the previous SOTA model, Cryslator, by 8.66% in coordinate prediction, and 45.16% in cell volume estimation. Figure 2 (a) shows the distribution of MAE for coordinates, lattice parameters, and cell volumes as predicted by the Dummy model and DeepRelax. DeepRelax demonstrates a notable leftward skewness in its distribution, signifying a tendency to predict structures that closely approach the relaxed state. To visualize the performance of Deeprelax, we take two typical structures, Sr₄Mn₂O₆ and Ba₁Mn₄O₈ from the X-Mn-O database (see Figure 3), and relax them using DeepRelax. As can be seen, the predicted structures are highly consistent with the DFT-relaxed ones. The results demonstrate close agreement with DFT-relaxed structures. More randomly selected samples are validated by DFT calculations in **Subsection 2.5**.

Table 1 Comparative results of DeepRelax and baseline models on the X-Mn-O dataset, based on MAE of coordinates (Å), bond length (Å), lattice (Å), cell volume (Å³), and match rate (%) between predicted and ground truth relaxed structures

Model	Coordinates	Bond length	Lattice	Cell volume	Match rate
Dummy	0.314	0.429	0.221	32.8	64.8
PAINN	0.159	0.175	0.066	3.8	81.2
EGNN	0.166	0.189	0.066	4.2	77.5
Cryslator*	0.127	-	-	6.2	83.7
DeepRelax	0.116	0.136	0.063	3.4	84.7

*The results of Cryslator are taken from [15]. DeepRelax is evaluated on the same training, validation, and testing sets as Cryslator for a fair comparison.

2.3 Benchmark on Materials Project

To demonstrate DeepRelax’s universal applicability across various elements of the periodic table and diverse crystal types, we conduct further evaluations using the Materials Project dataset[11]. This dataset spans 89 elements and comprises 187,687 snapshots from 62,783 compounds captured during their structural relaxation processes. By excluding compounds missing either initial or final structures, we refined the dataset to 62,724 pairs. Each pair consists of an initial and a corresponding final structure, providing a comprehensive basis for assessing the performance of DeepRelax. This dataset is then split into

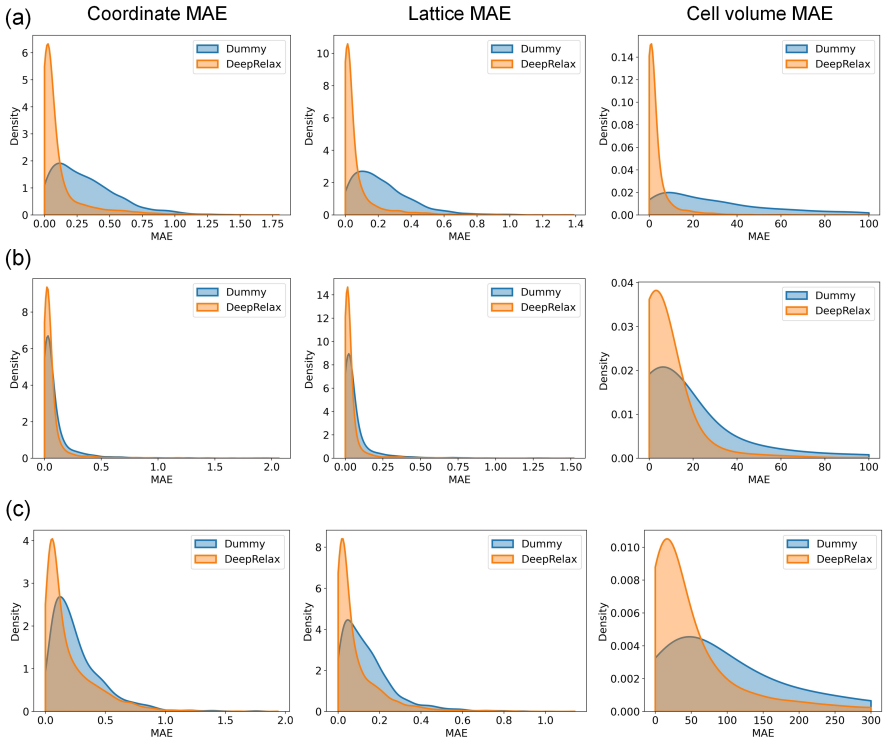


Fig. 2 Distribution of MAE for predicted structures by the Dummy model and DeepRelax across datasets: (a) X-Mn-O, (b) MP, and (c) C2DB. The subfigures display the MAE for coordinates, lattice parameters, and cell volumes, respectively.

training, validation, and test data in the ratio of 90%, 5%, and 5%, respectively. As illustrated in Figure S1, the structural differences for each pair tend toward a mean absolute error (MAE) of zero, indicating that many initial structures are closely aligned with their final counterparts.

Training a direct machine learning (ML) model for datasets with varied compositions poses significant challenges, as evidenced in CrysLator[21]. This model shows reduced prediction performance when trained on the diverse MP database. Despite these challenges, DeepRelax demonstrates its robustness and universality. As indicated in Table 2, DeepRelax significantly surpasses the three baseline models in coordinate prediction, highlighting its effectiveness even in diverse and complex datasets. Figure 2 (b) shows the MAE distribution for predicted structures compared to the ground truth for the MP dataset, which is less significant compared to the results for the X-Mn-O dataset shown in Figure 2 (a). This is because many initial structures closely resemble their final states in the MP database as evidenced by Figure S1. Consequently, the MP dataset presents a more complex learning challenge for structural relaxation models.

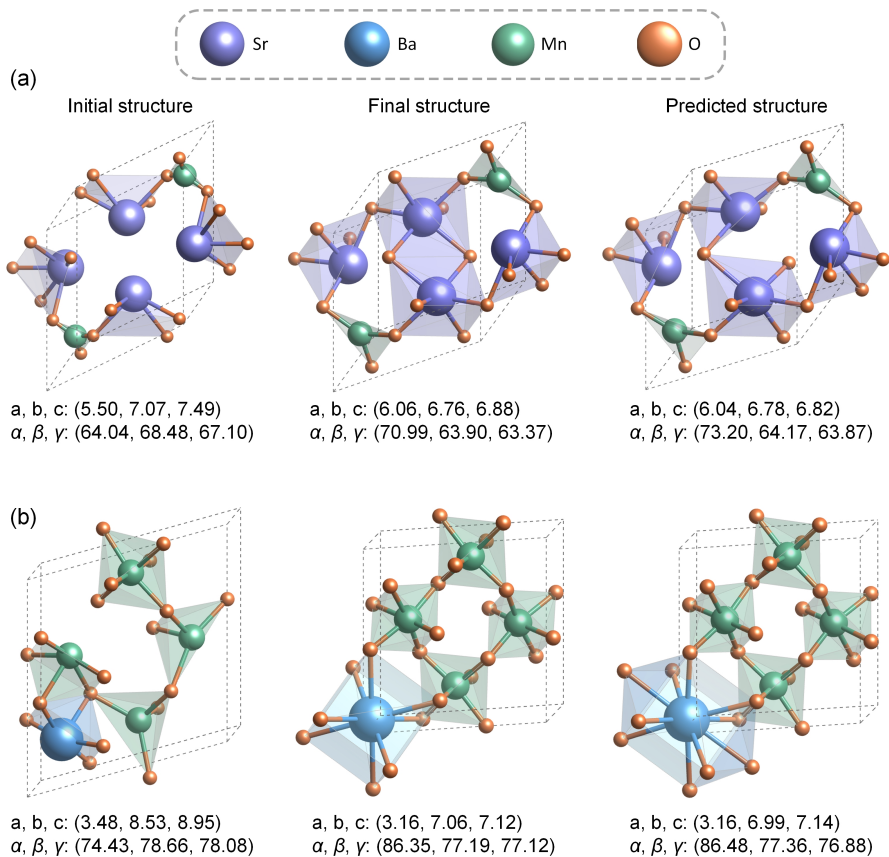


Fig. 3 Visualization of two crystal structures relaxed by DeepRelax: (a) $\text{Sr}_4\text{Mn}_2\text{O}_6$ and (b) $\text{Ba}_1\text{Mn}_4\text{O}_8$, where a, b, c, α , β , and γ are lattice constants. The results demonstrate close agreement with DFT-relaxed structures.

2.4 Transfer learning of pre-trained DeepRelax on Computational 2D Materials Database

Given that most materials databases do not provide the energy and force information of unrelaxed structures, it is difficult for conventional iterative ML models to transfer the trained model from Materials Project to other materials databases. This difficulty arises because transfer learning typically depends on the availability of energy and force information to fine-tune the model. DeepRelax, with its direct structural prediction feature, is more compatible with transfer learning, making it a flexible tool even when only structural data are available.

To demonstrate the universal application of DeepRelax, we extend the application of DeepRelax, initially pre-trained on 3D materials from the MP dataset, to 2D materials through transfer learning. We take the C2DB dataset [22–24] as an example, which covers 62 elements and comprises 11,581

Table 2 Comparison of results between the proposed DeepRelax and other models on the MP dataset. The improvement is calculated by comparing DeepRelax with the Dummy model

Model	Coordinates	Bond length	Lattice	Cell volume
Dummy	0.095	0.112	0.072	27.0
PAINN	0.088	0.082	0.043	9.3
EGNN	0.086	0.086	0.043	9.3
DeepRelax	0.066	0.094	0.041	9.6
Improvement	30.53%	16.07%	43.06%	64.44%

pairs of 2D crystal structures, each consisting of an initial and a final structure. The dataset is divided into training, validation, and testing subsets, maintaining a ratio of 6:2:2. The structural differences for each pair in this dataset fall within the range observed for the X-Mn-O and MP datasets, as shown in Figure S1.

In this context, DeepRelax trained via transfer learning is denoted as DeepRelaxT to differentiate it from DeepRelax. Table 3 illustrates our key findings: Firstly, both DeepRelax and DeepRelaxT outperform the other three baselines in the C2DB dataset, proving the applicability of our direct ML model to the system of 2D materials. Figure 2 (c) presents the MAE distribution for predicted structures by the Dummy model and DeepRelax on the C2DB dataset. These results suggest a modest improvement over the Dummy model for the C2DB dataset when compared to other datasets: the improvement is more significant than that observed for the MP dataset as depicted in Figure 2 (b). Secondly, DeepRelaxT demonstrates notable improvements over DeepRelax, with enhancements of 5.61% in coordinates, 38.43% in bond length, 3.53% in lattice, and 5.81% in cell volume in terms of MAE. Finally, DeepRelaxT shows a faster convergence rate than DeepRelax, as detailed in **SM Section 2**, Figure S2. These results underline the benefits of large-scale pretraining and the efficacy of transfer learning.

Table 3 Training DeepRelax on the C2DB dataset via transfer learning

Model	Coordinates	Bond length	Lattice	Cell volume
Dummy	0.268	0.400	0.142	149.6
PAINN	0.226	0.283	0.086	61.9
EGNN	0.232	0.311	0.089	67.9
DeepRelax	0.196	0.268	0.085	60.2
DeepRelaxT	0.185	0.165	0.082	56.7

2.5 DFT validations

We conduct a DFT validation of DeepRelax’s performance by comparing DFT calculated energy with the energy predicted by our model. To assess the predictive capability of our model under challenging conditions, we remove unrelaxed

structures from the X-Mn-O test set which are structurally similar to their corresponding final counterparts using Pymatgen’s Structure_matcher function. From the remaining test set ($N = 1,007$), we randomly selected 100 samples. Figure 4 (a) depicts the deviation distribution for the selected unrelaxed structures, which closely aligns with that of the complete test set, thereby affirming the representativeness of the selected subset.

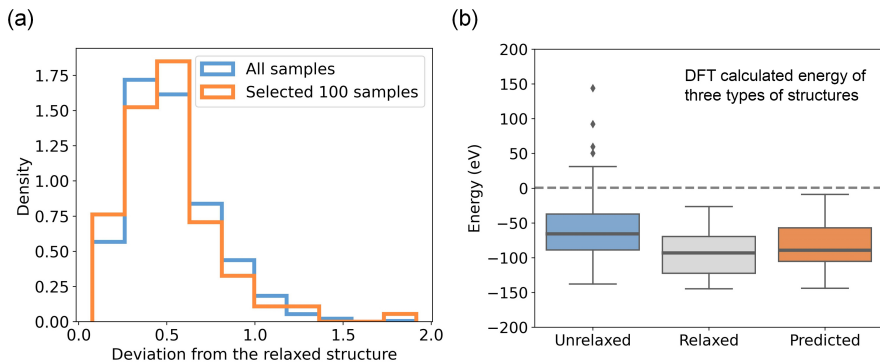


Fig. 4 (a) Histograms illustrating the density of deviations from the relaxed structure for the entire sample set and a selected subset of 100 samples, which demonstrates the subset’s representativeness. (b) Box plots illustrating the energy distributions for unrelaxed, DFT-relaxed, and DeepRelax-predicted structures, with the latter two exhibiting similar medians and spreads, confirming the accuracy of DeepRelax in approximating energetically favorable structures.

Subsequently, we employ DeepRelax to predict the relaxed structures for these samples. The energies of the unrelaxed, relaxed, and DeepRelax predicted structures are then calculated using DFT, as detailed in **Subsection 4.9**. Figure 4 (b) shows box plots of the energy distributions for the three structure categories. The predicted and relaxed structures have negative energy, and exhibit similar medians and interquartile ranges, suggesting that DeepRelax accurately predicts structures nearing their final ground states. This close alignment validates the model’s accuracy in predicting energetically favorable structures. The MAE in energy is significantly reduced by an order of magnitude from 32.51 for unrelaxed versus relaxed structures to only 5.97 for predicted versus relaxed structures.

2.6 Analysis of uncertainty

A critical challenge in integrating artificial intelligence into material discovery is establishing human trust in AI models. Current deep learning models typically offer reliable predictions only within the chemical space covered by their training datasets, known as the applicability domain[30]. Predictions for samples outside this domain can be unreliable. Thus, uncertainty quantification has become vital, enabling more trustworthy AI applications by quantifying

prediction confidence levels, thereby aiding researchers in decision-making and experimental planning.

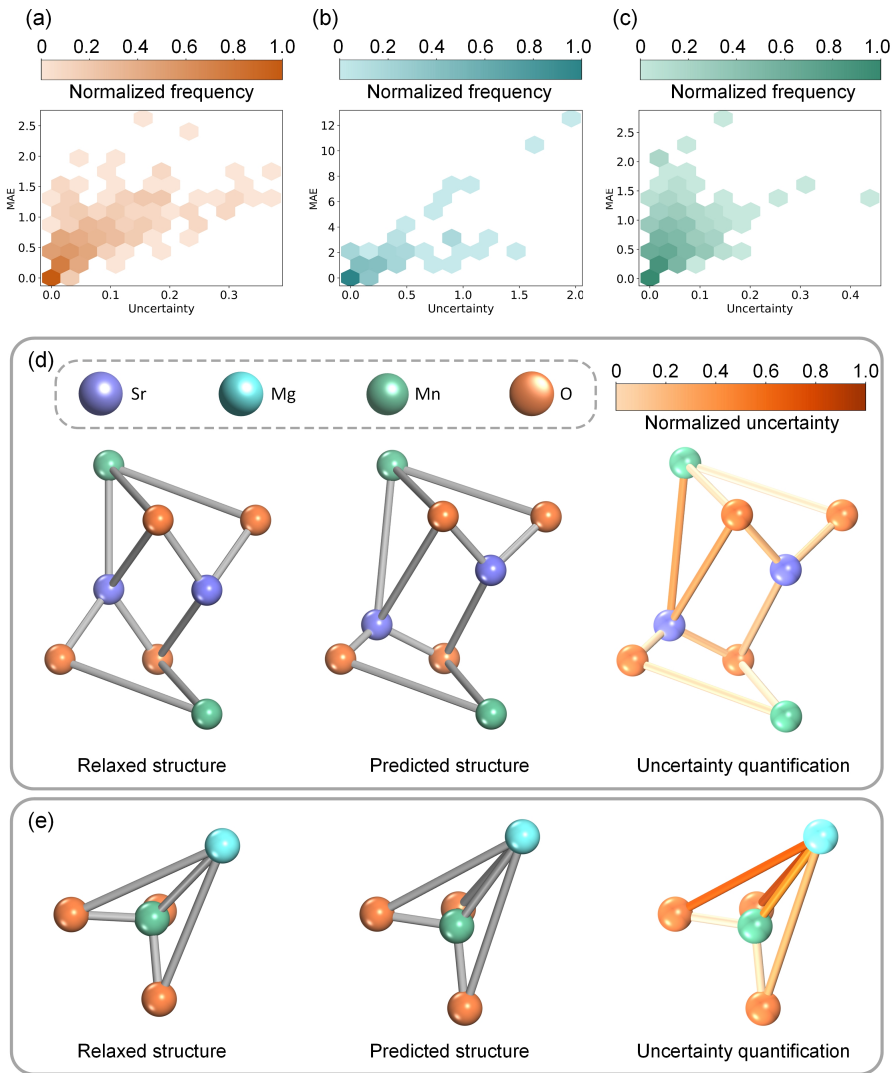


Fig. 5 Uncertainty quantification. Hexagonal binning plots comparing global uncertainty with distance MAE for the (a) X-Mn-O, (b) MP, and (c) C2DB datasets. Parts (d) and (e) of the figure illustrate the local uncertainty in the bond lengths of the predicted structures for Sr₂Mn₂O₄ and Mg₁Mn₁O₃, respectively, demonstrating the correlation between bond length prediction errors and their associated uncertainties.

To validate the efficacy of our proposed uncertainty quantification in reflecting the confidence level of model predictions, we compute Spearman's rank correlation coefficient between the predicted distance error and its associated

global uncertainty. Figures 5 (a), (b), and (c) show the hexagonal binning plots of global uncertainty against distance MAE for the X-Mn-O, MP, and C2DB datasets, respectively. Correlation coefficients of 0.95, 0.83, and 0.88 for these datasets demonstrate a strong correlation between predicted error and predicted global uncertainty. Figures 5 (d) and (e) present the local (bond-level) uncertainty visualization for two predicted structures, illustrating the correlation between predicted bond length error and associated uncertainty. These results indicate that the model’s predicted uncertainty is a reliable indicator of the predicted structure’s accuracy.

Table 4 Ablation study results showcasing the impact of PCOE and local uncertainty estimation on model performance.

Model	Coordinates	Bond length	Lattice	Cell volume
Dummy	0.314	0.429	0.221	32.839
Vanilla	0.155	0.170	0.063	3.478
DeepRelaxP	0.121	0.147	0.063	3.563
DeepRelaxU	0.142	0.171	0.064	3.539
DeepRelax	0.116	0.136	0.063	3.442

2.7 Ablation study

DeepRelax’s technical contributions are twofold: it utilizes periodic cell offset encoding (PCOE) for handling PBCs explicitly, and it employs a method for estimating local uncertainty (i.e., bond-level uncertainty).

To validate the effectiveness of these two strategies, we introduce three additional baseline models for comparison:

- **Vanilla**: Excludes both PCOE and local uncertainty estimation.
- **DeepRelaxP**: Integrates PCOE but omits local uncertainty estimation.
- **DeepRelaxU**: Implements local uncertainty estimation but not PCOE.

Table 4 demonstrates that DeepRelaxP attains a significant performance enhancement over the Vanilla model, suggesting the PCOE contributes greatly to model performance. On the other hand, DeepRelaxU shows a more modest improvement, which indicates the added value of local uncertainty estimation. Overall, DeepRelax shows a 25.16% improvement in coordinate MAE and a 20.00% advancement in bond length MAE over the Vanilla model. These comparative results underscore the combined effectiveness of positional PCOE and local uncertainty estimation in our final DeepRelax model.

3 Discussion

The rapid advancement of generative models like CDVAE[6], PGCGM[8], and MatterGen[7], has opened avenues for the prolific generation of hypothetical materials with potentially desirable properties, such as 2.2 million new materials recently discovered by Google DeepMind. Clearly, it is impossible to relax

such a huge number of structures using the traditional *ab initio* method, and it is also very difficult using the iterative ML relax models. For example, we further compare the efficiency between DeepRelax and M3GNet, a leading iterative ML model. DeepRelax offers a substantial speed advantage, being approximately 100 times faster than M3GNet (see **SM Section 3**, Table S1). Based on this estimation, to relax the 2.2 million new materials, our DeepRelax model only needs around 100 hours or 4 days, while M3GNet will take around 400 days. Moreover, our DeepRelax model supports parallel GPU processing, which can further significantly reduce computer time. Overall, we introduce a fast, scalable, and reliable deep generative model, DeepRelax, for direct structural relaxation. Despite its advancements, opportunities for further improvement remain, which we explore in subsequent discussions.

Firstly, DeepRelax primarily focuses on predicting interatomic distances, which are quantities fundamentally involving two-body interactions. Incorporating the prediction of higher-order many-body quantities could further enhance the accuracy of structural predictions.

Secondly, implementing active learning strategies[31, 32] may further enhance DeepRelax’s performance, particularly in underexplored chemical spaces. Active learning efficiently reduces the need for extensive training data by strategically choosing the most informative samples. DeepRelax’s capability to assess prediction uncertainty aligns well with the principles of active learning, suggesting its feasibility as a future enhancement method.

Thirdly, DeepRelax is not designed to replace DFT, but to significantly speed up the traditional *ab initio* relaxation process, especially for complex structures, such as complex chemical reaction surfaces or doped semiconductor interfaces.

In conclusion, DeepRelax represents a significant advancement in crystal structure prediction, offering efficient, scalable, universal, and trusted structural relaxation capabilities. It excels at direct predictions from initial configurations and effectively handles periodic boundary conditions, along with incorporating uncertainty quantification. DeepRelax thus stands as a powerful tool in advancing material science research.

4 Methods

4.1 Periodic structure of materials

Any material structure can be conceptualized as a periodic arrangement of atoms in 3D space[6]. This periodicity is typically captured by identifying a repeating unit, known as a unit cell, that effectively represents the material’s infinite structure. Such a unit cell, containing N atoms, can be fully characterized by three components:

- Atom Types: Represented by $\mathbf{A} = (a_0, \dots, a_N) \in \mathbb{A}^N$, where \mathbb{A} denotes the set of all chemical elements.
- Atom Coordinates: Denoted by $\mathbf{R} = (\vec{r}_0, \dots, \vec{r}_N) \in \mathbb{R}^{N \times 3}$.

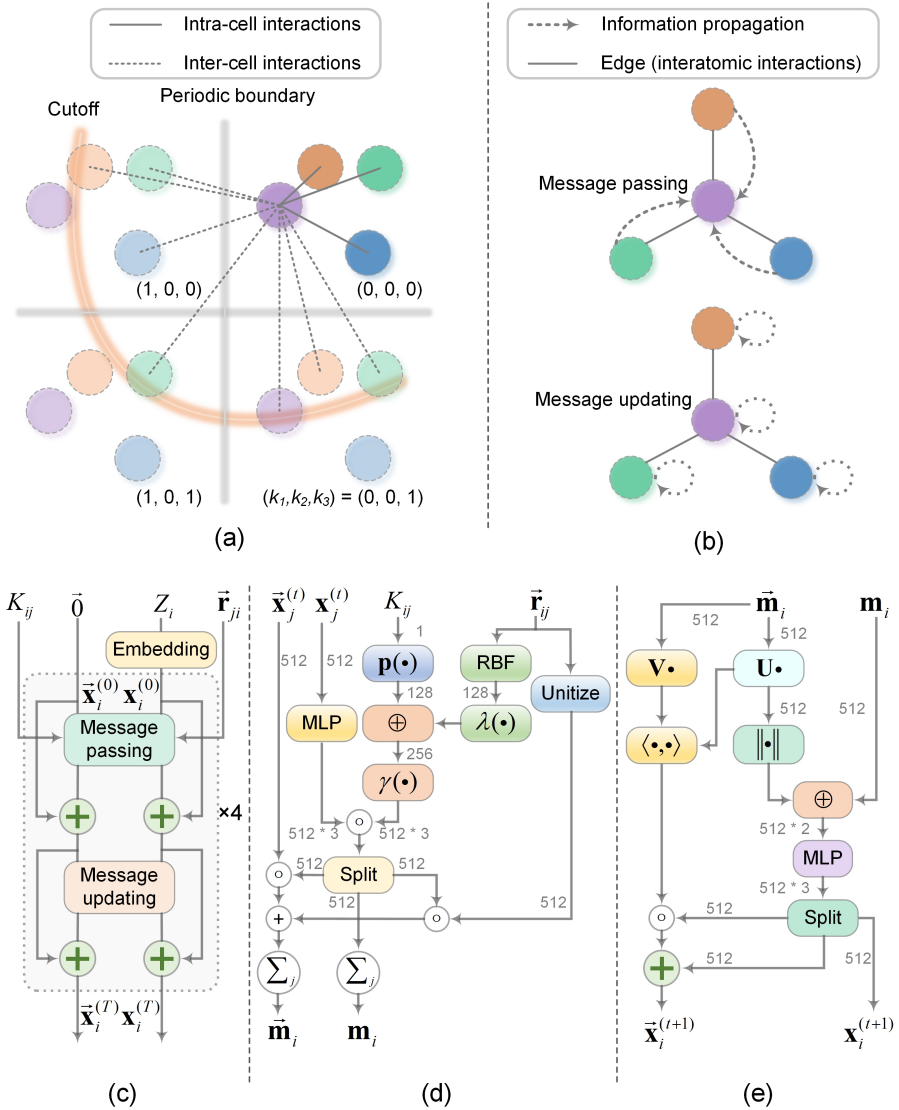


Fig. 6 The architecture of PaEGNN. (a) Illustrates the multi-graph representation designed to capture atomic interactions across cell boundaries in periodic structures. (b) Depicts an overview of PaEGNN, comprising four layers, each consisting of message passing and message updating phases. The specifics of these phases are further detailed in (d) and (e), respectively.

• Lattice Vectors: Expressed as $\mathbf{L} = (\vec{l}_1, \vec{l}_2, \vec{l}_3) \in \mathbb{R}^{3 \times 3}$.

Given $\mathbf{M} = (\mathbf{A}, \mathbf{R}, \mathbf{L})$, we can model the infinite periodic structure as:

$$\{(a'_i, \vec{r}'_i) | a'_i = a_i, \vec{r}'_i = \vec{r}_i + k_1 \vec{l}_1 + k_2 \vec{l}_2 + k_3 \vec{l}_3, k_1, k_2, k_3 \in \mathbb{Z}\}, \quad (1)$$

where (k_1, k_2, k_3) are the cell offsets used to replicate the unit cell across the 3D space.

4.2 Multi-graph representation for periodic structure

Multi-graphs offer an intuitive way to represent crystal structures under periodic boundary conditions (PBCs)[6], as depicted in Figure 6 (a). These graphs can be effectively processed by graph neural networks (GNNs) through graph convolutions or message passing, which simulate many-body interactions[11, 12, 26, 27, 33–55]. Formally, we define a multi-graph $\mathcal{G} = (\mathcal{V}, \mathcal{E})$ to encode these periodic structures. Here, $\mathcal{V} = \{v_1, \dots, v_N\}$ represents the set of nodes (atoms), and $\mathcal{E} = \{e_{ij, (k_1, k_2, k_3)} | i, j \in \{1, \dots, N\}, k_1, k_2, k_3 \in \mathbb{Z}\}$ signifies the set of edges (bonds). The edge $e_{ij, (k_1, k_2, k_3)}$ denotes a directed connection from node i in the original unit cell to node j in the cell translated by $k_1\vec{l}_1 + k_2\vec{l}_2 + k_3\vec{l}_3$. Nodes are interconnected with their nearest neighbors within a cutoff distance D (set to 6 Å in our study).

To actively explore the crystal symmetry, each node $v_i \in \mathcal{V}$ is assigned both a scalar feature $\mathbf{x}_i \in \mathbb{R}^F$ and a vector feature $\vec{\mathbf{x}}_i \in \mathbb{R}^{F \times 3}$, i.e., retaining F scalars and F vectors for each node. These features are updated in a way that preserves symmetry during training. The scalar feature $\mathbf{x}_i^{(0)}$ is initialized as an embedding dependent on the atomic number, $E(z_i) \in \mathbb{R}^F$, where z_i is the atomic number, and E is an embedding layer mapping z_i to a F -dimensional feature vector. This embedding is similar to the one-hot vector but is trainable. The vector feature is initially set to zero, $\vec{\mathbf{x}}_i^{(0)} = \vec{\mathbf{0}} \in \mathbb{R}^{F \times 3}$. Additionally, we define $\vec{\mathbf{r}}_{ij} = \vec{\mathbf{r}}_j - \vec{\mathbf{r}}_i$ as the vector from node v_i to v_j .

4.3 Periodicity-aware equivariant graph neural network

PaEGNN iteratively updates node representations in two phases: message passing and updating. These phases are illustrated in Figure 6 (b) and further detailed in Figures 6 (c), (d), and (e). During message passing, nodes receive information from neighboring nodes, expanding their accessible radius. In the updating phase, PaEGNN utilizes the node’s internal messages (composed of F scalars and F vectors) to update its features. To prevent over-smoothing[56, 57], skip connections are added to each layer.

In subsequent sections, we define the norm $\|\cdot\|$ and dot product $\langle \cdot, \cdot \rangle$ as operations along the spatial dimension, while concatenation \oplus and the Hadamard product \circ are performed along the feature dimension.

4.3.1 Periodic cell offset encoding

A notable feature of PaEGNN, distinguishing it from previous models[26, 36], is the explicit differentiation of atoms in various cells to encode PBCs. To achieve this, we define the set $\mathcal{C} = \{-2, -1, 0, 1, 2\}$. We then use this set to generate translated cells with offsets $(k_1, k_2, k_3) \in \mathcal{C} \times \mathcal{C} \times \mathcal{C}$. The translated cells, resulting from the offsets $(k_1, k_2, k_3) \in \mathcal{C} \times \mathcal{C} \times \mathcal{C}$, are generally sufficient

to encompass all atoms within a 6 Å cutoff distance. We use $(k_1, k_2, k_3)_{ij}$ to denote the cell offset from node i to node j , where node j is located in a cell translated by $k_1\vec{l}_1 + k_2\vec{l}_2 + k_3\vec{l}_3$ relative to node i . Let $K_{ij} = (k_1 + 2) + (k_2 + 2)5 + (k_3 + 2)25$ be a positive integer that uniquely indexes the cell offset, the sinusoidal positional encoding[58] for K_{ij} is computed as:

$$p(K_{ij}, f) = \begin{cases} \sin(K_{ij}/10000^{f/F}), & \text{if } f \in \{0, 2, 4, \dots, F-2\} \\ \cos(K_{ij}/10000^{(f-1)/F}), & \text{if } f \in \{1, 3, 5, \dots, F-1\} \end{cases} \quad (2)$$

The full positional encoding vector is then

$$\mathbf{p}(K_{ij}) = (p(K_{ij}, 0), p(K_{ij}, 1), \dots, p(K_{ij}, F-1)) \in \mathbb{R}^F \quad (3)$$

The periodic cell offset encoding $\mathbf{p}(K_{ij})$ explicitly indicates node j 's cell location relative to node i . This encoding enables the GNN to explicitly recognize the periodic structure, thereby enhancing predictive performance.

4.3.2 Message passing phase

During this phase, a node v_i aggregates messages from neighboring scalars \mathbf{x}_j and vectors $\vec{\mathbf{x}}_j$, forming intermediate scalar and vector variables \mathbf{m}_i and $\vec{\mathbf{m}}_i$ as follows:

$$\mathbf{m}_i = \sum_{v_j \in \mathcal{N}(v_i)} (\mathbf{W}_h \mathbf{x}_j^{(t)}) \circ \gamma_h(\lambda(\|\vec{\mathbf{r}}_{ji}\|) \oplus \mathbf{p}(K_{ji})) \quad (4)$$

$$\begin{aligned} \vec{\mathbf{m}}_i = & \sum_{v_j \in \mathcal{N}(v_i)} (\mathbf{W}_u \mathbf{x}_j^{(t)}) \circ \gamma_u(\lambda(\|\vec{\mathbf{r}}_{ji}\|) \oplus \mathbf{p}(K_{ij})) \circ \vec{\mathbf{x}}_j^{(t)} \\ & + (\mathbf{W}_v \mathbf{x}_j^{(t)}) \circ \gamma_v(\lambda(\|\vec{\mathbf{r}}_{ji}\|) \oplus \mathbf{p}(K_{ij})) \circ \frac{\vec{\mathbf{r}}_{ji}}{\|\vec{\mathbf{r}}_{ji}\|} \end{aligned} \quad (5)$$

Here, \oplus denotes concatenation, $\mathcal{N}(v_i)$ represents the neighboring nodes of v_i , $\mathbf{W}_h, \mathbf{W}_u, \mathbf{W}_v \in \mathbb{R}^{F \times F}$ are trainable weight matrices, λ is a set of Gaussian radial basis functions (RBF)[38] that are used to expand bond distances, and γ_h, γ_u , and γ_v are a linear projection mapping the concatenated feature back to F -dimensional space.

4.3.3 Message updating phase

The updating phase concentrates on integrating the F scalars and F vectors within \mathbf{m}_i and $\vec{\mathbf{m}}_i$ to generate updated scalar $\mathbf{x}_i^{(t+1)}$ and vector $\vec{\mathbf{x}}_i^{(t+1)}$:

$$\mathbf{x}_i^{(t+1)} = \mathbf{W}_{s1}(\mathbf{m}_i \oplus \|\mathbf{U}\vec{\mathbf{m}}_i\|) + \mathbf{W}_{s2}(\mathbf{m}_i \oplus \|\mathbf{U}\vec{\mathbf{m}}_i\|) \langle \mathbf{V}\vec{\mathbf{m}}_i, \mathbf{U}\vec{\mathbf{m}}_i \rangle \quad (6)$$

$$\vec{\mathbf{x}}_i^{(t+1)} = \mathbf{W}_v(\mathbf{m}_i \oplus \|\mathbf{U}\vec{\mathbf{m}}_i\|) \circ (\mathbf{V}\vec{\mathbf{m}}_i) \quad (7)$$

where $\mathbf{W}_{s1}, \mathbf{W}_{s2}, \mathbf{W}_v \in \mathbb{R}^{F \times 2F}$ and $\mathbf{U}, \mathbf{V} \in \mathbb{R}^{F \times F}$.

4.4 Predicting relaxation quantities

Assuming PaEGNN comprises T layers, we define $\mathbf{h}_{ij} = \gamma(\lambda(\|\vec{\mathbf{r}}_{ji}\|) \oplus \mathbf{p}(k_1, k_2, k_3))$. The prediction of a pair-wise distance \hat{d}_{ij} and its corresponding local uncertainty \hat{u}_{ij} for the edge $e_{ij,(k_1,k_2,k_3)}$ is formulated as:

$$\hat{d}_{ij} = |f_d(\mathbf{W}_n \mathbf{x}_i^{(T)} \oplus \mathbf{W}_n \mathbf{x}_j^{(T)} \oplus \mathbf{h}_{ij})| \quad (8)$$

$$\hat{u}_{ij} = f_u(\mathbf{W}_n \mathbf{x}_i^{(T)} \oplus \mathbf{W}_n \mathbf{x}_j^{(T)} \oplus \mathbf{h}_{ij}) \quad (9)$$

where $\mathbf{W}_n \in \mathbb{R}^{F \times F}$ is a learnable matrix, and $f_d, f_u : \mathbb{R}^{3F} \rightarrow \mathbb{R}$ are linear maps. Using Eqn. (8) and (9), we can predict both the interatomic distances in the relaxed structure and the displacements between the initial and relaxed structures, along with their respective local uncertainties.

DeepRelax predicts the lattice matrix as follows:

$$\hat{\mathbf{L}} = r_L \left(f_L(\mathbf{W}_l(\vec{\mathbf{l}}_1 \oplus \vec{\mathbf{l}}_2 \oplus \vec{\mathbf{l}}_3) \oplus \left(\sum_{v_i \in \mathcal{G}} \mathbf{W}_x \mathbf{x}_i \right)) \right) \quad (10)$$

Here, $\mathbf{W}_x \in \mathbb{R}^{F \times F}$, $\mathbf{W}_l \in \mathbb{R}^{9 \times F}$, and $f_L : \mathbb{R}^{2F} \rightarrow \mathbb{R}^9$ is a linear mapping yielding a 9-dimensional vector \mathbf{L}_v . The operation r_L reshapes \mathbf{L}_v into a 3×3 matrix $\hat{\mathbf{L}}$ to reflect the lattice vectors.

4.5 Uncertainty-aware loss function

To quantify aleatoric uncertainty[30, 59], DeepRelax is trained to minimize an uncertainty-aware loss \mathcal{L} , comprising interatomic distance loss \mathcal{L}_i , displacement loss \mathcal{L}_d , and lattice loss \mathcal{L}_l :

$$\mathcal{L}_i = \sum_{e_{ij,(k_1,k_2,k_3)} \in \mathcal{E}} \log(2\hat{u}_{ij}) + \frac{|\hat{d}_{ij} - d_{ij}|}{\hat{u}_{ij}} \quad (11)$$

$$\mathcal{L}_d = \sum_{e_{ij,(0,0,0)} \in \mathcal{E}} \log(2\hat{u}_{ij}) + \frac{|\hat{d}_{ij} - d_{ij}|}{\hat{u}_{ij}} \quad (12)$$

$$\mathcal{L}_l = |\hat{\mathbf{L}} - \mathbf{L}| \quad (13)$$

$$\mathcal{L} = \mathcal{L}_i + \mathcal{L}_d + \mathcal{L}_l \quad (14)$$

In these expressions, d_{ij} and \mathbf{L} represent the ground truth distance and lattice matrix of the relaxed structure, respectively. The edges $e_{ij,(k_1,k_2,k_3)} \in \mathcal{E}$ pertain to interatomic distance predictions, whereas $e_{ij,(0,0,0)} \in \mathcal{E}$ denotes edges used for displacement predictions within the unit cell, discounting PBCs.

Minimizing \mathcal{L}_i and \mathcal{L}_d is mathematically equal to maximize the Laplace log-likelihood as:

$$\log p(x|\mu, b) = -\log(2b) - \frac{|x - \mu|}{b} \quad (15)$$

where μ and b are the mean and variance of the Laplace log-likelihood, respectively. Therefore, minimizing \mathcal{L}_i and \mathcal{L}_d encourages the output distances to follow a distribution akin to the Laplace log-likelihood, where \hat{d}_{ij} is the mean and \hat{u}_{ij} is the variance. Consequently, a larger \hat{u}_{ij} indicates greater local uncertainty in the prediction, and vice versa.

4.6 Numerical Euclidean distance geometry solver

We propose a numerical EDG solver to determine the relaxed structure that aligns with the predicted relaxation quantities. Specifically, for a given graph $\mathcal{G} = (\mathcal{V}, \mathcal{E}, d)$ and a dimension K , the EDG problem[60–62] seeks a realization—specifically, a coordinate matrix $\hat{\mathbf{R}} \in \mathbb{R}^{N \times K} : \mathcal{V} \rightarrow \mathbb{R}^K$ in K -dimensional space that satisfy the distance constraint d as follows:

$$\forall (u, v) \in \mathcal{E}, \|\hat{\mathbf{R}}(u) - \hat{\mathbf{R}}(v)\| = d_{uv} \quad (16)$$

For simplicity, $\hat{\mathbf{R}}(u)$ and $\hat{\mathbf{R}}(v)$ are typically written as $\hat{\mathbf{R}}_u$ and $\hat{\mathbf{R}}_v$.

We reformulate the conventional EDG problem into a global optimization task:

$$\mathcal{L}_g = \sum_{(u,v) \in \mathcal{E}} \left| \|\hat{\mathbf{R}}_u - \hat{\mathbf{R}}_v\| - d_{uv} \right| \quad (17)$$

This is a non-convex optimization problem and minimizing \mathcal{L}_g gives an approximation solution of $\hat{\mathbf{R}}$.

In our context, we aim to find a coordinate matrix $\hat{\mathbf{R}} \in \mathbb{R}^{N \times 3}$ for a system of N atoms in three-dimensional space, meeting the constraints imposed by \hat{d}_{ij} , \hat{u}_{ij} , and $\hat{\mathbf{L}}$. Specifically, we first define an upper bound and lower bound using \hat{d}_{ij} , \hat{u}_{ij} as follows:

$$\hat{d}_{ij}^u = \hat{d}_{ij} + \exp(\hat{u}_{ij}) \quad (18)$$

$$\hat{d}_{ij}^l = \hat{d}_{ij} - \exp(\hat{u}_{ij}) \quad (19)$$

Subsequently, we propose minimizing a bounded Euclidean distance (BED) loss:

$$\mathcal{L}_g = \sum_{\substack{e_{ij, (k_1, k_2, k_3)} \in \mathcal{E} \\ e_{ij, (0, 0, 0)} \in \mathcal{E}}} \max(0, \|\hat{\mathbf{R}}_u - \hat{\mathbf{R}}_v\| - \hat{d}_{ij}^u) + \sum_{\substack{e_{ij, (k_1, k_2, k_3)} \in \mathcal{E} \\ e_{ij, (0, 0, 0)} \in \mathcal{E}}} \max(0, \hat{d}_{ij}^l - \|\hat{\mathbf{R}}_u - \hat{\mathbf{R}}_v\|) \quad (20)$$

For each edge $e_{ij, (k_1, k_2, k_3)}$, the location of node j is dictated by $k_1 \hat{\mathbf{l}}_1 + k_2 \hat{\mathbf{l}}_2 + k_3 \hat{\mathbf{l}}_3$, where $\hat{\mathbf{l}}_1$, $\hat{\mathbf{l}}_2$, $\hat{\mathbf{l}}_3$ are predicted lattice vectors. The BED loss only penalizes coordinate pairs whose distances fall outside the lower and upper bounds, thus mitigating the impact of less accurate predictions. In our work, we use Adam optimizer[63] to minimize \mathcal{L}_g .

4.7 Uncertainty quantification

We use global uncertainty to assess the reliability of the predicted structure. This involves training an ensemble of T independent model replicates, with

$M = 5$ used in this study, a method that has been extensively validated for effective uncertainty estimation [30, 64]. The T model replicates had the same neural network architectures and hyperparameters, but the learnable parameters were initialized with different random seeds. For the t -th model replicate, let $\hat{d}_{ij}(t)$ denote the predicted distance and $\hat{u}_{ij}(t)$ the local uncertainty. The global uncertainty, \hat{U} , is computed as follows:

$$\hat{U}_a = \left(\frac{1}{N} \sum_{\substack{e_{ij,(k_1,k_2,k_3)} \in \mathcal{E} \\ e_{ij,(0,0,0)} \in \mathcal{E}}} \left(\frac{1}{T} \sum_{t=1}^T \exp(\hat{u}_{ij}(t)) \right) \right)^2 \quad (21)$$

$$\bar{d}_{ij} = \frac{1}{T} \sum_{t=1}^T \hat{d}_{ij}(t) \quad (22)$$

$$\hat{U}_e = \frac{1}{N} \sum_{\substack{e_{ij,(k_1,k_2,k_3)} \in \mathcal{E} \\ e_{ij,(0,0,0)} \in \mathcal{E}}} \left(\frac{1}{T} \sum_{t=1}^T (\hat{d}_{ij}(t) - \bar{d}_{ij})^2 \right) \quad (23)$$

$$\hat{U} = \hat{U}_a + \hat{U}_e \quad (24)$$

In these equations, N represents the total number of distance pairs. The terms \hat{U}_a and \hat{U}_e are known as aleatoric and epistemic uncertainties, respectively[59].

4.8 Implementation details

The DeepRelax model is implemented using PyTorch. Experiments are conducted on an NVIDIA RTX A6000 with 48 GB of memory. The training objective is to minimize Eqn. (14). We use the AdamW optimizer[65] with a learning rate of 0.0001 to update the model's parameters. Additionally, we implement a learning rate decay strategy, reducing the learning rate if there is no improvement in a specified metric for a duration of 5 epochs.

We implement PAINN[26] and EGNN[27] models, utilizing the source code available at <https://github.com/Open-Catalyst-Project/ocp> and <https://github.com/vgsatorras/egnn>, respectively. These equivariant models are adept at directly predicting the coordinates of a relaxed structure from its unrelaxed counterpart, leveraging the intrinsic property that coordinates are equivariant quantities.

4.9 DFT calculations

In our study, DFT calculations are performed using the Vienna Ab initio Simulation Package (VASP)[66], employing the generalized gradient approximation (GGA) with the Perdew-Burke-Ernzerhof (PBE) exchange-correlation functional[67]. We set the energy cut-off to 550 eV, the energy convergence criterion to 1.0×10^{-5} eV, and the K-point mesh to a $9 \times 9 \times 9$ grid, ensuring precise total energy calculations. The effective on-site Coulomb interactions (U value) of Mn 3d orbital is chosen as 3.9 eV, aligning with that used in

Cryslator[15]. For high-throughput self-consistent calculations, we utilize the AiiDA computational framework[68, 69].

4.10 Performance indicators

4.10.1 MAE of coordinate

The MAE of coordinates assesses the structural difference between the predicted and actual relaxed structures. It is defined as:

$$\Delta_{\text{coord}} = \sum_{v_i \in \mathcal{G}} |\hat{\mathbf{r}}_i - \vec{\mathbf{r}}_i| \quad (25)$$

where $\hat{\mathbf{r}}_i$, $\vec{\mathbf{r}}_i$ represent the predicted and ground truth Cartesian coordinates, respectively.

4.10.2 MAE of bond length

The MAE of bond length measures the error in predicting interatomic distances:

$$\Delta_{\text{bond}} = \sum_{e_{ij, (k_1, k_2, k_3)} \in \mathcal{E}} |\hat{d}_{ij} - d_{ij}| \quad (26)$$

where \hat{d}_{ij} , d_{ij} are the predicted and ground interatomic distances.

4.10.3 MAE of lattice

This metric calculates the error in predicting the lattice parameters:

$$\Delta_{\text{lattice}} = |\hat{\mathbf{L}} - \mathbf{L}| \quad (27)$$

where $\hat{\mathbf{L}}$ and \mathbf{L} are the predicted and ground lattice parameters.

4.10.4 MAE of cell volume

The error in predicting the cell volume is given by:

$$\Delta_{\text{volume}} = |\hat{\mathbf{l}}_1 \cdot (\hat{\mathbf{l}}_2 \times \hat{\mathbf{l}}_3)| - |\vec{\mathbf{l}}_1 \cdot (\vec{\mathbf{l}}_2 \times \vec{\mathbf{l}}_3)| \quad (28)$$

where \times is the cross product, and $\hat{\mathbf{l}}_i$ and $\vec{\mathbf{l}}_i$ are the predicted and ground truth lattice vectors.

4.10.5 Match rate

We utilize the 'Structure_matcher' function from the Pymatgen package[1] to compare the predicted relaxed structure with the ground truth relaxed structure. Default parameters are used for this function (ltol=0.2, stol=0.3) to ensure consistent and objective comparisons.

Conflicts of interest

The authors declare that they have no competing interests.

Acknowledgements

We acknowledge Prof. Kristian Sommer Thygesen and Peder Lyngby for their generous provision of the C2DB database, complete with both initial and final structures. This work was supported by the National Natural Science Foundation of China (Grant No. 62176272), Research and Development Program of Guangzhou Science and Technology Bureau (No. 2023B01J1016), Key-Area Research and Development Program of Guangdong Province (No. 2020B1111100001), Singapore MOE Tier 1 (No. A-8001194-00-00), and Singapore MOE Tier 2 (No. A-8001872-00-00).

References

- [1] Ong, S.P., Richards, W.D., Jain, A., Hautier, G., Kocher, M., Cholia, S., Gunter, D., Chevrier, V.L., Persson, K.A., Ceder, G.: Python materials genomics (pymatgen): A robust, open-source python library for materials analysis. *Computational Materials Science* **68**, 314–319 (2013)
- [2] Saal, J.E., Kirklin, S., Aykol, M., Meredig, B., Wolverton, C.: Materials design and discovery with high-throughput density functional theory: the open quantum materials database (oqmd). *Jom* **65**, 1501–1509 (2013)
- [3] Curtarolo, S., Setyawan, W., Hart, G.L., Jahnatek, M., Chepulskii, R.V., Taylor, R.H., Wang, S., Xue, J., Yang, K., Levy, O., *et al.*: Aflow: An automatic framework for high-throughput materials discovery. *Computational Materials Science* **58**, 218–226 (2012)
- [4] Zhou, J., Shen, L., Costa, M.D., Persson, K.A., Ong, S.P., Huck, P., Lu, Y., Ma, X., Chen, Y., Tang, H., *et al.*: 2dmatpedia, an open computational database of two-dimensional materials from top-down and bottom-up approaches. *Scientific data* **6**(1), 86 (2019)
- [5] Chen, B., Conway, L.J., Sun, W., Kuang, X., Lu, C., Hermann, A.: Phase stability and superconductivity of lead hydrides at high pressure. *Physical Review B* **103**(3), 035131 (2021)
- [6] Xie, T., Fu, X., Ganea, O.-E., Barzilay, R., Jaakkola, T.: Crystal diffusion variational autoencoder for periodic material generation. arXiv preprint arXiv:2110.06197 (2021)
- [7] Zeni, C., Pinsler, R., Zügner, D., Fowler, A., Horton, M., Fu, X., Shysheya, S., Crabbé, J., Sun, L., Smith, J., *et al.*: Mattergen: a generative model for inorganic materials design. arXiv preprint arXiv:2312.03687 (2023)

- [8] Zhao, Y., Siriwardane, E.M.D., Wu, Z., Fu, N., Al-Fahdi, M., Hu, M., Hu, J.: Physics guided deep learning for generative design of crystal materials with symmetry constraints. *npj Computational Materials* **9**(1), 38 (2023)
- [9] Merchant, A., Batzner, S., Schoenholz, S.S., Aykol, M., Cheon, G., Cubuk, E.D.: Scaling deep learning for materials discovery. *Nature* **624**(7990), 80–85 (2023)
- [10] Zuo, Y., Qin, M., Chen, C., Ye, W., Li, X., Luo, J., Ong, S.P.: Accelerating materials discovery with bayesian optimization and graph deep learning. *Materials Today* **51**, 126–135 (2021)
- [11] Chen, C., Ong, S.P.: A universal graph deep learning interatomic potential for the periodic table. *Nature Computational Science* **2**(11), 718–728 (2022)
- [12] Deng, B., Zhong, P., Jun, K., Riebesell, J., Han, K., Bartel, C.J., Ceder, G.: Chgnet as a pretrained universal neural network potential for charge-informed atomistic modelling. *Nature Machine Intelligence*, 1–11 (2023)
- [13] Mosquera-Lois, I., Kavanagh, S.R., Ganose, A.M., Walsh, A.: Machine-learning structural reconstructions for accelerated point defect calculations. *arXiv preprint arXiv:2401.12127* (2024)
- [14] Kolluru, A., Shuaibi, M., Palizhati, A., Shoghi, N., Das, A., Wood, B., Zitnick, C.L., Kitchin, J.R., Ulissi, Z.W.: Open challenges in developing generalizable large-scale machine-learning models for catalyst discovery. *ACS Catalysis* **12**(14), 8572–8581 (2022)
- [15] Kim, S., Noh, J., Jin, T., Lee, J., Jung, Y.: A structure translation model for crystal compounds. *npj Computational Materials* **9**(1), 142 (2023)
- [16] Yoon, J., Ulissi, Z.W.: Differentiable optimization for the prediction of ground state structures (dogss). *Physical Review Letters* **125**(17), 173001 (2020)
- [17] Wang, Z., Wang, X., Luo, X., Gao, P., Sun, Y., Lv, J., Wang, H., Wang, Y., Ma, Y.: Concurrent learning scheme for crystal structure prediction. *Physical Review B* **109**(9), 094117 (2024)
- [18] Omeo, S.S., Wei, L., Hu, M., Hu, J.: Crystal structure prediction using neural network potential and age-fitness pareto genetic algorithm. *Journal of Materials Informatics* **4**(1), 2 (2024). <https://doi.org/10.20517/jmi.2023.33>
- [19] Belsky, A., Hellenbrandt, M., Karen, V.L., Luksch, P.: New developments

- in the inorganic crystal structure database (icsd): accessibility in support of materials research and design. *Acta Crystallographica Section B: Structural Science* **58**(3), 364–369 (2002)
- [20] Jain, A., Ong, S.P., Hautier, G., Chen, W., Richards, W.D., Dacek, S., Cholia, S., Gunter, D., Skinner, D., Ceder, G., et al.: Commentary: The materials project: A materials genome approach to accelerating materials innovation. *APL materials* **1**(1) (2013)
- [21] Kim, S., Noh, J., Gu, G.H., Aspuru-Guzik, A., Jung, Y.: Generative adversarial networks for crystal structure prediction. *ACS central science* **6**(8), 1412–1420 (2020)
- [22] Haastrup, S., Strange, M., Pandey, M., Deilmann, T., Schmidt, P.S., Hinsche, N.F., Gjerding, M.N., Torelli, D., Larsen, P.M., Riis-Jensen, A.C., et al.: The computational 2d materials database: high-throughput modeling and discovery of atomically thin crystals. *2D Materials* **5**(4), 042002 (2018)
- [23] Gjerding, M.N., Taghizadeh, A., Rasmussen, A., Ali, S., Bertoldo, F., Deilmann, T., Knøsgaard, N.R., Kruse, M., Larsen, A.H., Manti, S., et al.: Recent progress of the computational 2d materials database (c2db). *2D Materials* **8**(4), 044002 (2021)
- [24] Lyngby, P., Thygesen, K.S.: Data-driven discovery of 2d materials by deep generative models. *npj Computational Materials* **8**(1), 232 (2022)
- [25] Noh, J., Kim, S., ho Gu, G., Shinde, A., Zhou, L., Gregoire, J.M., Jung, Y.: Unveiling new stable manganese based photoanode materials via theoretical high-throughput screening and experiments. *Chemical Communications* **55**(89), 13418–13421 (2019)
- [26] Schütt, K., Unke, O., Gastegger, M.: Equivariant message passing for the prediction of tensorial properties and molecular spectra. In: *International Conference on Machine Learning*, pp. 9377–9388 (2021). PMLR
- [27] Satorras, V.G., Hoogeboom, E., Welling, M.: E (n) equivariant graph neural networks. In: *International Conference on Machine Learning*, pp. 9323–9332 (2021). PMLR
- [28] Zhang, X., Zhang, O., Shen, C., Qu, W., Chen, S., Cao, H., Kang, Y., Wang, Z., Wang, E., Zhang, J., et al.: Efficient and accurate large library ligand docking with karmadock. *Nature Computational Science* **3**(9), 789–804 (2023)
- [29] Dong, T., Yang, Z., Zhou, J., Chen, C.Y.-C.: Equivariant flexible modeling of the protein–ligand binding pose with geometric deep learning. *Journal*

of Chemical Theory and Computation (2023)

- [30] Yu, J., Wang, D., Zheng, M.: Uncertainty quantification: Can we trust artificial intelligence in drug discovery? *Iscience* (2022)
- [31] Tran, K., Ulissi, Z.W.: Active learning across intermetallics to guide discovery of electrocatalysts for co₂ reduction and h₂ evolution. *Nature Catalysis* **1**(9), 696–703 (2018)
- [32] Szymanski, N.J., Rendy, B., Fei, Y., Kumar, R.E., He, T., Milsted, D., McDermott, M.J., Gallant, M., Cubuk, E.D., Merchant, A., *et al.*: An autonomous laboratory for the accelerated synthesis of novel materials. *Nature* **624**(7990), 86–91 (2023)
- [33] Gasteiger, J., Becker, F., Günnemann, S.: Gemnet: Universal directional graph neural networks for molecules. *Advances in Neural Information Processing Systems* **34**, 6790–6802 (2021)
- [34] Li, H., Wang, Z., Zou, N., Ye, M., Xu, R., Gong, X., Duan, W., Xu, Y.: Deep-learning density functional theory hamiltonian for efficient ab initio electronic-structure calculation. *Nature Computational Science* **2**(6), 367–377 (2022)
- [35] Zhong, Y., Yu, H., Su, M., Gong, X., Xiang, H.: Transferable equivariant graph neural networks for the hamiltonians of molecules and solids. *npj Computational Materials* **9**(1), 182 (2023)
- [36] Xie, T., Grossman, J.C.: Crystal graph convolutional neural networks for an accurate and interpretable prediction of material properties. *Physical review letters* **120**(14), 145301 (2018)
- [37] Park, C.W., Wolverton, C.: Developing an improved crystal graph convolutional neural network framework for accelerated materials discovery. *Physical Review Materials* **4**(6), 063801 (2020)
- [38] Schütt, K., Kindermans, P.-J., Sauceda Felix, H.E., Chmiela, S., Tkatchenko, A., Müller, K.-R.: SchNet: A continuous-filter convolutional neural network for modeling quantum interactions. *Advances in neural information processing systems* **30** (2017)
- [39] Chen, C., Ye, W., Zuo, Y., Zheng, C., Ong, S.P.: Graph networks as a universal machine learning framework for molecules and crystals. *Chemistry of Materials* **31**(9), 3564–3572 (2019)
- [40] Gasteiger, J., Groß, J., Günnemann, S.: Directional message passing for molecular graphs. In: *International Conference on Learning Representations (ICLR)* (2020)

- [41] Choudhary, K., DeCost, B.: Atomistic line graph neural network for improved materials property predictions. *npj Computational Materials* **7**(1), 185 (2021)
- [42] Unke, O.T., Chmiela, S., Gastegger, M., Schütt, K.T., Sauceda, H.E., Müller, K.-R.: Spookynet: Learning force fields with electronic degrees of freedom and nonlocal effects. *Nature communications* **12**(1), 7273 (2021)
- [43] Pablo-García, S., Morandi, S., Vargas-Hernández, R.A., Jorner, K., Ivković, Ž., López, N., Aspuru-Guzik, A.: Fast evaluation of the adsorption energy of organic molecules on metals via graph neural networks. *Nature Computational Science*, 1–10 (2023)
- [44] Batzner, S., Musaelian, A., Sun, L., Geiger, M., Mailoa, J.P., Kornbluth, M., Molinari, N., Smidt, T.E., Kozinsky, B.: E (3)-equivariant graph neural networks for data-efficient and accurate interatomic potentials. *Nature communications* **13**(1), 2453 (2022)
- [45] Banik, S., Dhabal, D., Chan, H., Manna, S., Cherukara, M., Molinero, V., Sankaranarayanan, S.K.: Cegann: Crystal edge graph attention neural network for multiscale classification of materials environment. *npj Computational Materials* **9**(1), 23 (2023)
- [46] Unke, O.T., Meuwly, M.: Physnet: A neural network for predicting energies, forces, dipole moments, and partial charges. *Journal of chemical theory and computation* **15**(6), 3678–3693 (2019)
- [47] Wang, L., Liu, Y., Lin, Y., Liu, H., Ji, S.: Comenet: Towards complete and efficient message passing for 3d molecular graphs. *Advances in Neural Information Processing Systems* **35**, 650–664 (2022)
- [48] Zhang, X., Zhou, J., Lu, J., Shen, L.: Interpretable learning of voltage for electrode design of multivalent metal-ion batteries. *npj Computational Materials* **8**(1), 175 (2022)
- [49] Gilmer, J., Schoenholz, S.S., Riley, P.F., Vinyals, O., Dahl, G.E.: Neural message passing for quantum chemistry. In: *International Conference on Machine Learning*, pp. 1263–1272 (2017). PMLR
- [50] Louis, S.-Y., Zhao, Y., Nasiri, A., Wang, X., Song, Y., Liu, F., Hu, J.: Graph convolutional neural networks with global attention for improved materials property prediction. *Physical Chemistry Chemical Physics* **22**(32), 18141–18148 (2020)
- [51] Fuchs, F., Worrall, D., Fischer, V., Welling, M.: Se (3)-transformers: 3d roto-translation equivariant attention networks. *Advances in neural information processing systems* **33**, 1970–1981 (2020)

- [52] Brandstetter, J., Hesselink, R., van der Pol, E., Bekkers, E.J., Welling, M.: Geometric and physical quantities improve e (3) equivariant message passing. In: International Conference on Learning Representations (2021)
- [53] Dai, M., Demirel, M.F., Liang, Y., Hu, J.-M.: Graph neural networks for an accurate and interpretable prediction of the properties of polycrystalline materials. *npj Computational Materials* **7**(1), 103 (2021)
- [54] Omee, S.S., Louis, S.-Y., Fu, N., Wei, L., Dey, S., Dong, R., Li, Q., Hu, J.: Scalable deeper graph neural networks for high-performance materials property prediction. *Patterns* (2022)
- [55] Haghightlari, M., Li, J., Guan, X., Zhang, O., Das, A., Stein, C.J., Heidar-Zadeh, F., Liu, M., Head-Gordon, M., Bertels, L., *et al.*: Newtonnet: A newtonian message passing network for deep learning of interatomic potentials and forces. *Digital Discovery* **1**(3), 333–343 (2022)
- [56] Yang, Z., Zhong, W., Lv, Q., Chen, C.Y.-C.: Learning size-adaptive molecular substructures for explainable drug–drug interaction prediction by substructure-aware graph neural network. *Chemical Science* **13**(29), 8693–8703 (2022)
- [57] Yang, Z., Zhong, W., Zhao, L., Chen, C.Y.-C.: Mgraphdta: deep multi-scale graph neural network for explainable drug–target binding affinity prediction. *Chemical science* **13**(3), 816–833 (2022)
- [58] Vaswani, A., Shazeer, N., Parmar, N., Uszkoreit, J., Jones, L., Gomez, A.N., Kaiser, L., Polosukhin, I.: Attention is all you need. *Advances in neural information processing systems* **30** (2017)
- [59] Kendall, A., Gal, Y.: What uncertainties do we need in bayesian deep learning for computer vision? *Advances in neural information processing systems* **30** (2017)
- [60] Liberti, L., Lavor, C., Maculan, N., Mucherino, A.: Euclidean distance geometry and applications. *SIAM review* **56**(1), 3–69 (2014)
- [61] Lu, W., Wu, Q., Zhang, J., Rao, J., Li, C., Zheng, S.: Tankbind: Trigonometry-aware neural networks for drug-protein binding structure prediction. *Advances in neural information processing systems* **35**, 7236–7249 (2022)
- [62] Masters, M.R., Mahmoud, A.H., Wei, Y., Lill, M.A.: Deep learning model for efficient protein–ligand docking with implicit side-chain flexibility. *Journal of Chemical Information and Modeling* **63**(6), 1695–1707 (2023)
- [63] Kingma, D.P., Ba, J.: Adam: A method for stochastic optimization. *arXiv*

preprint arXiv:1412.6980 (2014)

- [64] Luo, Y., Liu, Y., Peng, J.: Calibrated geometric deep learning improves kinase–drug binding predictions. *Nature Machine Intelligence*, 1–12 (2023)
- [65] Loshchilov, I., Hutter, F.: Decoupled weight decay regularization. arXiv preprint arXiv:1711.05101 (2017)
- [66] Kresse, G., Furthmüller, J.: Efficient iterative schemes for ab initio total-energy calculations using a plane-wave basis set. *Physical review B* **54**(16), 11169 (1996)
- [67] Perdew, J.P., Burke, K., Ernzerhof, M.: Generalized gradient approximation made simple. *Physical review letters* **77**(18), 3865 (1996)
- [68] Huber, S.P., Zoupanos, S., Uhrin, M., Talirz, L., Kahle, L., Häuselmann, R., Gresch, D., Müller, T., Yakutovich, A.V., Andersen, C.W., *et al.*: Aiida 1.0, a scalable computational infrastructure for automated reproducible workflows and data provenance. *Scientific data* **7**(1), 300 (2020)
- [69] Uhrin, M., Huber, S.P., Yu, J., Marzari, N., Pizzi, G.: Workflows in aiida: Engineering a high-throughput, event-based engine for robust and modular computational workflows. *Computational Materials Science* **187**, 110086 (2021)